JOURNAL OF AIRCRAFT
Vol. 44, No. 1, January–February 2007

Aircraft Geometry Design and Optimization for Sonic Boom Reduction

Sriram K. Rallabhandi* and Dimitri N. Mavris†
Georgia Institute of Technology, Atlanta, Georgia 30332-0150

DOI: 10.2514/1.20456

An improved approach for conceptual supersonic aircraft design is developed and presented. The proposed approach consists of two basic elements: 1) geometry parameterization and discretization, and 2) improved linearized analyses. The geometry generation and discretization scheme creates arbitrarily refined, unstructured geometries quickly and efficiently. Improved linearized tools allow geometric effects to be better captured than existing linearized analysis. The geometry generation and improved linear analyses are coupled to a shape optimization procedure to obtain the geometric shape parameters that simultaneously optimize sonic boom intensity on the ground and lift to drag ratio. Results of this preliminary optimization are presented and discussed.

Nomenclature

AD^2	=	Anderson–Darling test statistic
C_D	=	drag coefficient
C_F	=	skin friction coefficient
C_{Flam}	=	laminar skin friction coefficient
C_{Fturb}	=	turbulent skin friction coefficient
C_L	=	lift coefficient
$d_1, d_2, \ldots, d_m$	=	discrete configuration variables
$\frac{d}{l}$	=	fuselage fineness ratio
F_0	=	cumulative distribution function of the assumed distribution
H	=	flight altitude, ft
h	=	nonuniform rational B-splines definition homogenous coordinate
L	=	characteristic length
l	=	aircraft length, ft
l_f	=	fuselage length, ft
M	=	Mach number
N	=	statistical sample size
nm	=	nautical mile
P_c	=	critical probability parameter
Re	=	Reynolds number
S_1	=	heuristic in Anderson–Darling test
$s_1, s_2, \ldots, s_n$	=	continuous shape parameters
T	=	ambient atmospheric temperature
$\frac{t}{c}$	=	thickness to chord ratio
t_i	=	nose nonuniform rational B-splines control point parameters
x	=	x coordinate
x_c	=	transition location
x_n	=	angle of attack corrected axial locations
y	=	y coordinate
z	=	z coordinate
α	=	blend crossover relaxation parameter
α_a	=	angle of attack, deg
γ	=	genetic algorithm blend crossover parameter
θ	=	azimuthal angle
μ	=	Mach angle, $\sin^{-1}(1/M)$
χ	=	temperature gradient parameter

Received 10 October 2005; revision received 7 August 2006; accepted for publication 15 September 2006.

*Research Engineer II, Aerospace Systems Design Laboratory, Daniel Guggenheim School of Aerospace Engineering. Member AIAA.

†Boeing Professor of Advanced Aerospace Systems Analysis and Director, Aerospace Systems Design Laboratory, Daniel Guggenheim School of Aerospace Engineering. Associate Fellow AIAA.

I. Introduction and Motivation

ACCORDING to various market studies [1,2], there is a renewed interest for designing an efficient, low-noise airplane that can travel at supersonic speeds over land to achieve the projected benefits of faster travel. However, federal aviation regulations (FAR) prohibit civilian aircraft from flying at supersonic speeds over the United States. The main reason for this regulation is the intense sonic boom created by such a flight. If the sonic boom strength is reduced to an acceptable level and the technical feasibility proved, the regulations may be changed. An in-depth explanation of sonic boom modeling is beyond the scope of this paper; excellent reviews have been published by Carlson and Maglieri [3], Seebass [4], and Whitham [5]. Conceptual sonic boom modeling relies on equivalent area and linearized atmospheric pressure propagation. The near-field pressure signature is obtained using analysis involving the calculation of the volume and lift disturbances due to the supersonic flight of the aircraft. This pressure signature is then propagated to the ground using linearized acoustics principles analogous to geometric optics.

In the initial stages of design, analysis tools used are fast and robust to quickly analyze the vast design space. This large space of configurations has to be narrowed down to a few suitable geometries to be passed on to the preliminary design stages. Traditional methods, because of their extremely fast turnaround time, consume insignificant computational resources. However, in most cases, the results are achieved at the cost of accuracy and design uncertainty. Conceptual sonic boom analysis studies [6–8] use linearized methods in their design process. Traditional linearized methods such as AWAVE [9,10] (wave drag and equivalent area due to volume calculation), ARAP [11] (linear pressure propagation), and PBOOM [12] produce inaccurate equivalent area distribution [13] for most geometries because the geometry is represented as a collection of disjoint surfaces. Deviations from the accurate equivalent area distribution have a significant impact on the F function [5] and the magnitude of shocks in the ground signature. To demonstrate this, deviations are introduced in a sample equivalent area distribution. This baseline equivalent area distribution is obtained from the extension [13] to the sonic boom minimizing theory of Seebass–George–Darden [14,15]. The area distribution perturbations along with a baseline curve are shown in Fig. 1. The perturbations are quite benign compared with the baseline equivalent area distribution. The F-function distribution corresponding to each of the cases is calculated from the second derivative of the equivalent area and is shown in Fig. 2. A slight perturbation in the area below the baseline curve causes an expansion followed by a compression in the near field. As the signature propagates through the atmosphere, the

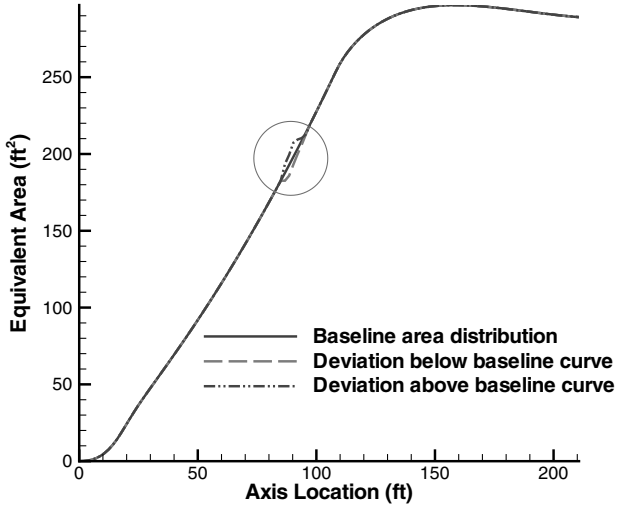

Fig. 1 Area perturbations.

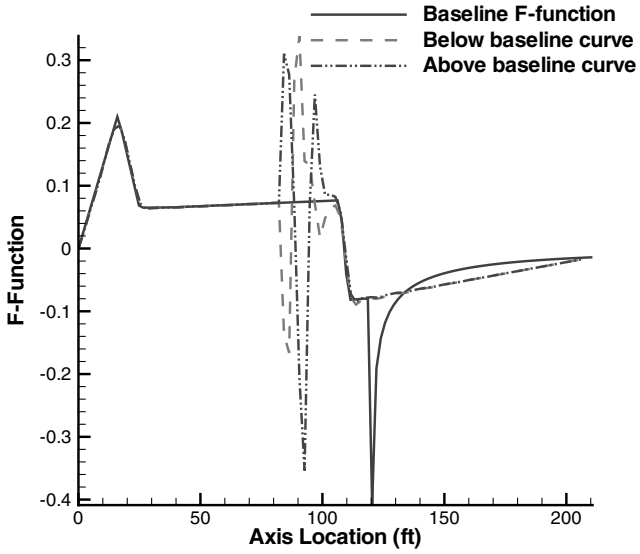

Fig. 2 Comparison of *F* functions corresponding to perturbed area distributions.

compression moves forward and is reduced in strength as it meets the expansion wave. Thus, coalescence with the front shock is avoided, or the compression strength magnitude is reduced. In contrast, if the perturbation is above the baseline curve, the near field has a compression followed by an expansion. Because compressions travel faster than expansions, this compression has a far greater chance of merging with the front shock system. Figure 3 compares the ground shock signatures in all three cases by propagating the *F* function through the atmosphere. PCBOOM [16] is used for all propagation results used in this study. It is a modification of the waveform parameter method of Thomas [17]. A hyperbolic tangent shock structure is assumed to obtain the shock rise times and loudness values. Referring to Fig. 3, the shock strength values for the area deviation below the baseline curve are less than the corresponding values for the case in which there is deviation above the baseline curve. These results indicate that seemingly small errors in the computation of the equivalent area distribution have a significant impact on ground pressure signatures. This limitation is overlooked when using linearized tools because accuracy is not desired in the conceptual stages; just ballpark estimates.

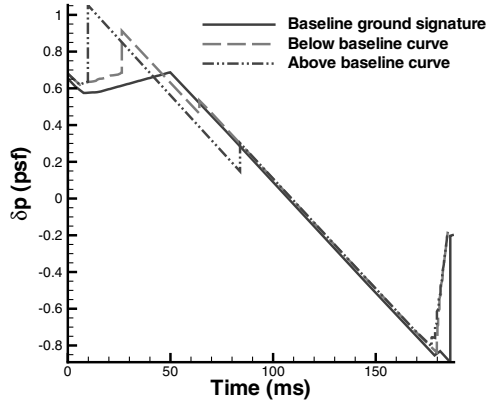

Fig. 3 Comparison of ground signatures corresponding to perturbed area distributions.

There is a desire to use improved fidelity analyses with the intent of improving accuracy and reducing uncertainty associated with using lower fidelity analyses. This desire has been formulated into a design philosophy [18] according to which various levels of analysis fidelity need to be used as the design progresses. If varying levels of fidelity for analyses have to be used, the generated geometry should be suitable for all these levels. To capture the complex three dimensional effects in the near field of the aircraft, computational fluid dynamics (CFD) simulation has to be carried out, which requires a surface discretized watertight geometry. Watertight in this context means not only no gaps between surface grid cells of a particular component, but also no gaps between grid cells of adjoining components. This means that component intersections should be evaluated using numerical schemes to mimic solid modeling methods of a high end CAD package.

A broad existing hierarchy of aerodynamic evaluation, in the increasing order of complexity, is 1) conceptual methods, 2) panel methods, 3) Euler CFD, and 4) Navier–Stokes CFD. A fundamental disconnect exists between the conceptual and other aerodynamic analyses in terms of the geometry format used. Existing linearized tools yield poor results for many configurations in the design space for supersonic aircraft. Computational fluid dynamics can be used to improve the prediction of near-field equivalent area distribution. Unfortunately, it is computationally very expensive and probably not worth the effort to use CFD throughout the optimization process in the conceptual stages, where the shape of the configuration has to be selected from a significantly large domain. There have been efforts in the past [19,20] to run nonlinear codes over conceptual geometries. These methods, however, are limited in their applicability. This paper focuses on improving the conceptual geometry representation and analysis tools for supersonic aircraft design; sonic boom minimization is chosen as the application example. This improved geometry representation provides a bridge between conceptual, low-fidelity and detailed, high-fidelity analyses. This procedure allows consistent analyses over a common geometry. The novelties of the proposed approach with regard to sonic boom modeling are the ability to obtain equivalent area due to volume without resorting to any geometric assumptions, and the potential to readily run CFD analysis on conceptual geometries. A genetic algorithm is used to demonstrate a shape optimization procedure. This is intended to be a simple demonstration of including the geometry representation and the associated analyses into an optimization setting. Two objectives are considered; sonic boom intensity on the ground and the lift-to-drag ratio. The sonic boom intensity is calculated as perceived loudness level in decibels (PLdB). This metric is calculated using the method laid out by Stevens [21] and takes into effect the sensitivity of the human ear to varying loudness levels.

II. Geometry Modeling

An efficient shape parameterization strategy for geometry generation is a prerequisite for performing aerodynamic shape optimization. There is a rich body of research investigating how to create efficient parametric geometries. Bloor and Wilson [22] introduce a partial differential equation approach to obtaining arbitrary aircraft configurations by solving a biharmonic partial

Table 1 Discrete parameters

Component	Component type parameter					
	0	1	2	3	4	5
Fuselage (d_1)	No fuselage	Nose specified using Bezier curve	Full fuselage using Bezier curves	NURBS nose, rest-Bezier curves	Fuselage in cross sections	Area ruled fuselage
Wing (d_2)	No wing	Conventional	Delta	Double-delta	Multisection	Swing-wing
H-Tail (d_3)	No H-tail	Canard	Conventional	T-tail	T-tail + Canard	
V-Tail (d_4)	No V-tail	Conventional				
Engine (d_5)	No engines	Wing mounted, 2 below wing	Fuselage mounted	Wing mounted, 2 above wing	Wing mounted, 4 below wing	

Table 2 Important continuous parameters

Component	Important continuous parameters
Fuselage	Length, maximum diameter, max. diameter location, bezier control points for nose, midsection and aft region, camber, camber location, bluntness parameter, parameters for nonaxisymmetric nose section
Wing	Wing location, t/c, camber, camber location, twist distribution, dihedral, Bezier control points for leading edge, sweep, span
H-tail	Aspect ratio, taper ratio, sweep, t/c, longitudinal location, vertical location
V-tail	Aspect ratio, taper ratio, sweep, t/c, longitudinal location
Engine	Engine location, radius, hub to tip ratio, engine length

Table 3 Fuselage and wing continuous parameters

Component	Setting	Variables
Fuselage (d_1)	1	s_1–s_{16}
	2	s_1–s_{16}
	3	s_1–s_{19}
	4	s_1–s_{21}
	5	s_1–s_{12}
Wing (d_2)	1	s_{m1}–s_{m1+10}
	2	s_{m1}–s_{m1+8}
	3	s_{m1}–s_{m1+17}
	4	s_{m1}–s_{m1+18}
	5	s_{m1}–s_{m1+10}
	6	s_{m1}–s_{m1+18}

differential equation (PDE). Smith et al. [23] extend the PDE approach to generate arbitrary configurations along with volume grid generation and grid sensitivity. Various geometry generation tools and their important features are presented by Kerr et al. [24]. Samareh [25,26] provides an excellent compilation of different shape parameterization techniques. These techniques, though very useful to the creation of mathematically closed surfaces in further stages of design, consume a significant setup and computational time and do not cater to the needs of the conceptual design, which are the ability to consider a wide range of shapes and to rapidly evaluate performance metrics for each such shape. We have developed a geometry generation and discretization method to create geometries quickly and efficiently. The underlying idea of this geometry generation scheme is to use design variables to control the shape as well as the configuration of each component of the aircraft. Shape in this context refers to the curvature, twist, dihedral, and other local features of the aircraft components. Configuration variables (d_m) signify the presence or absence of components, and the number of components. The configuration variables have discrete settings and different values for these produce different types of components as shown in Table 1. For example, depending on the value of discrete wing parameter, the wing geometry is a conventional, delta, double-delta, multisection or a swing–wing design. In addition, within each configuration, there are various continuous parameters to define the shape of each component. Table 2 presents some of the continuous parameters. Included here are various planform parameters, control points for nonuniform rational B-splines (NURBS) surfaces and Bezier curves. These parameters for different components constitute the continuous variable vector s_n. The number of continuous parameters associated with each component change with the configuration variable setting. Table 3 presents the continuous parameters in terms of s_n corresponding to the fuselage and the wing. According to this, if the fuselage discrete parameter setting takes a value of 2, there are 16 continuous parameters associated with that setting, whereas if it is 4, then there are 21 variables to represent the fuselage. If the wing discrete parameter setting is 4, then there are 19 continuous parameters defining the wing; and $m1$ in s_{m1} depends on the number of continuous parameters defining the fuselage. If a particular aircraft shape has $d_1 = 3$ and $d_2 = 5$, then $m1$ takes on a value of 20. This logic is extended to other components to decide the combined variable list for the whole aircraft.

The use of NURBS surfaces in creating aircraft nose shapes is demonstrated in this paragraph. Variables such as cabin diameter (Cdia) cabin length and five random parameters $t_i \in (0, 1)$, $i = 1 \ldots 5$ are used to generate the control points with the definitions given in Fig. 4. The camber function (Camb) of the nose cone is a quadratic expression with input parameter t_4. The coefficients of the quadratic camber expression are derived by imposing zero camber at the first and last nose sections as well a variable camber value at a variable camber location between the first and last nose sections. The axial locations y and z represent the Cartesian coordinates of the control points. These parameters are used so as to give a varying cross-section shape to the nose. The control points are then used to generate a cubic NURBS surface. A sample nose cone is shown in Fig. 5 along with the control points. The middle and aft sections of the fuselage are assumed to be axisymmetric with circular cross sections. These sections are generated using Bezier curves with control points as the design variables with proper conditions at the boundaries of adjoining sections to guarantee smoothness across sections. Fuselage shapes produced by the formulation include axisymmetric rear sections with pointed or blunt nose cones.

Wing shape parameters include twist, camber, control points for leading and trailing edge Bezier curves and other parameters that are simply the dimensions and planform locations of components. Figure 6 shows three different wing planforms obtained using Bezier

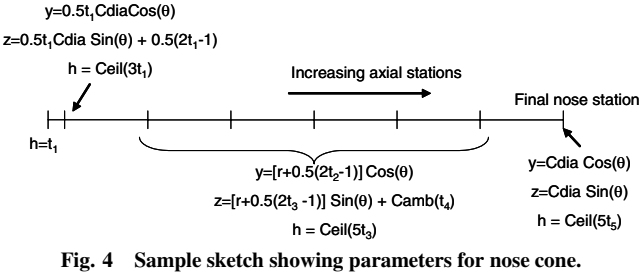

Fig. 4 Sample sketch showing parameters for nose cone.

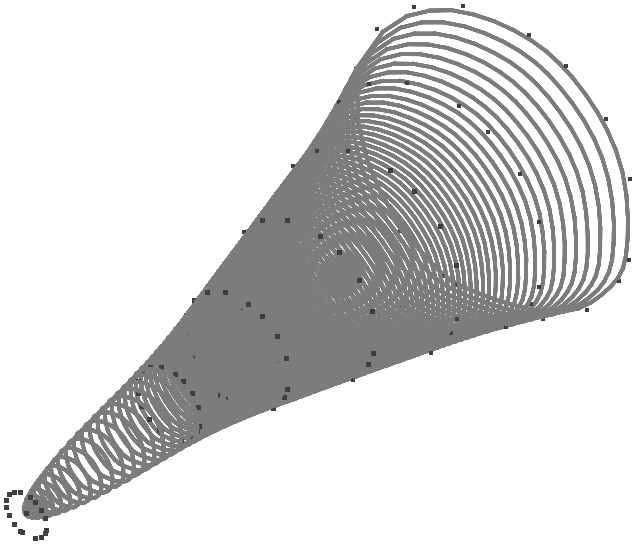

Fig. 5 Sample nose cone using NURBS definition.

control points as design variables for the leading and trailing edges. Additional parameters such as thickness to chord ratio, leading edge radius, camber location, root chord, tip chord, and planform area are used to create detailed wing definitions. Other components of the aircraft are similarly parameterized. The maximum number of parameters used to define a complete geometry is 75. Parametric decomposition and local shape control of individual components are achieved by representing the geometry in terms of a combination of discrete and continuous variables.

The configurations obtained by using the preceding parameterization strategy are not readily suitable for high-fidelity analysis. Our desired goal of discretization scheme is a geometry suitable for CFD and other analysis. To carry out surface intersections, the wire-frame geometry generated using parameters is refined to ensure better quality surface mesh. The refining procedure progressively introduces cross sections and computes the aspect ratio of the quadrilaterals. The refining process is terminated once the aspect ratio of all the quadrilaterals is less than or equal to a target value set by the user. Figure 7 shows a geometry created by the geometry engine along with a refined version of the same geometry. The geometry representation does not have component intersection information at this stage.

The next stage in geometry modeling is to obtain component intersections. The GNU triangulated surface library (GTS) [27] is used to perform the geometric Boolean operations. GTS library consists of data structures for efficient manipulation of surfaces

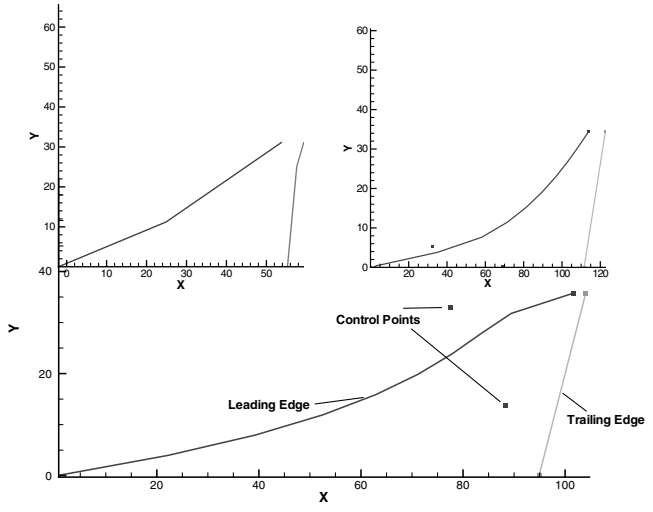

Fig. 6 Sample wing planforms using Bezier control points.

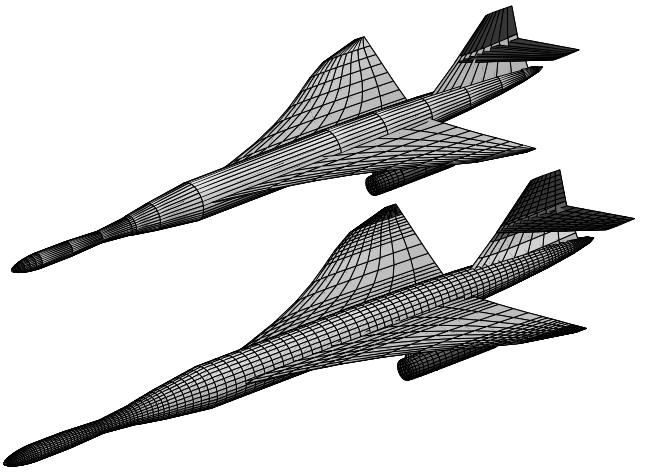

Fig. 7 Wire-frame geometry and its refined counterpart.

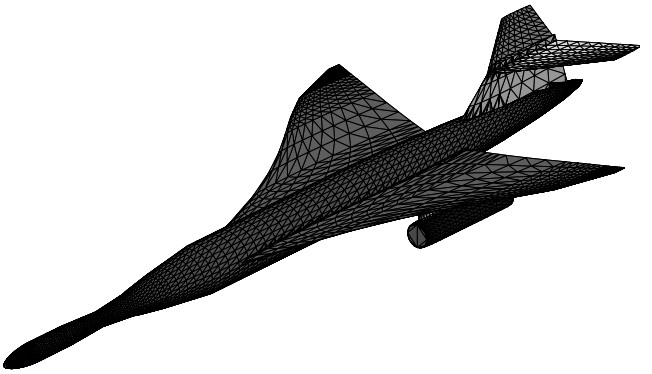

Fig. 8 Fully triangulated aircraft.

including union and intersection based on constrained Delaunay triangulation algorithm [28]. The geometry obtained using the combination of discrete and continuous variables is read into GTS data structures. Each component is triangulated, "sealed," and placed on a stack. Depending on the location of components on the stack, they are taken in turn and combined together two at a time using GTS Boolean operations. If a certain combination does not intersect a component in the stack, the next component is tried. This procedure is continued until all the components in the stack are used up. The final result of these geometric operations is shown in Fig. 8. The generated configuration provides a basic geometry platform on which different aerodynamic analyses can be run. To run CFD, the initial surface grid connectivity is used to create a volume mesh around the body of interest and the flowfield around the body is solved. The surfaces of the discretized geometry are distinguished from each other by using a different color for each component. This makes it easy in the later stages of design if the mesh over a particular component, for example wing, has to be refined without disturbing the mesh resolution over other components. It is also useful if a particular component (e.g., the wing) is subject to a boundary condition different from other components. An example of imposing different boundary conditions occurs in the simulation of blowing or suction over wings. A meshed surface geometry is achieved very quickly on a desktop computer. This procedure provides adequate flexibility to the configuration designer to change the shape or configuration of different components of the aircraft.

III. Modified Equivalent Area Estimation

Changes to the geometry format necessitate modifications to the existing linearized methods. Some of the existing linearized methods for sonic boom prediction are modified to make use of the improved geometry representation. These are explained in the following sections.

A. Volume Contribution and Wave Drag

According to slender body theory and equivalent body assumption, wave drag calculation [29] requires the average area computed from several azimuthal Mach planes whereas sonic boom calculation requires an area from a single Mach plane oriented at an azimuthal angle of −90 deg. This is because, for sonic boom calculation, only disturbances traveling exactly below the aircraft are needed, whereas for wave drag, contributions from all directions are required. The computational procedure used in this study discretizes the aircraft axis to user specified resolution and Mach planes passing through these axial locations are used to obtain the intercepted areas of the aircraft at these locations. To orient the Mach planes corresponding to the azimuthal angles, rotation and translation matrices [30] are used. The equivalent area due to volume [31] is computed by using the geometry created by the shape parameters and GTS.

The results from the Mach-plane intersection of GTS geometries need to be validated. The first validation case is a Sears–Haack body of length 30 ft and volume 100 ft^3. The area predicted using GTS geometry matches exactly with the analytical expressions for the area distribution of the Sears–Haack body. Figure 9 depicts a sample wing-body-canard geometry used as a second example. Figure 10 shows the equivalent area due to volume corresponding to the geometry in Fig. 9 for a Mach number of 1.4. AWAVE produces a distribution that overpredicts the values in the wing-body

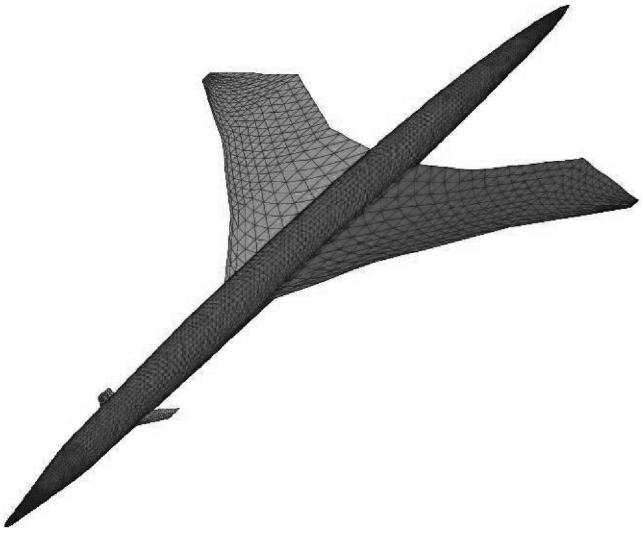

Fig. 9 Sample wing-body-canard geometry.

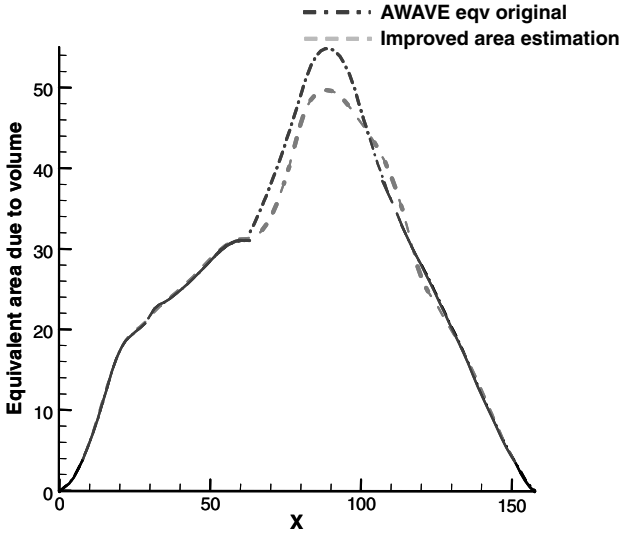

Fig. 10 Equivalent area due to volume comparison on a wing-body-canard geometry.

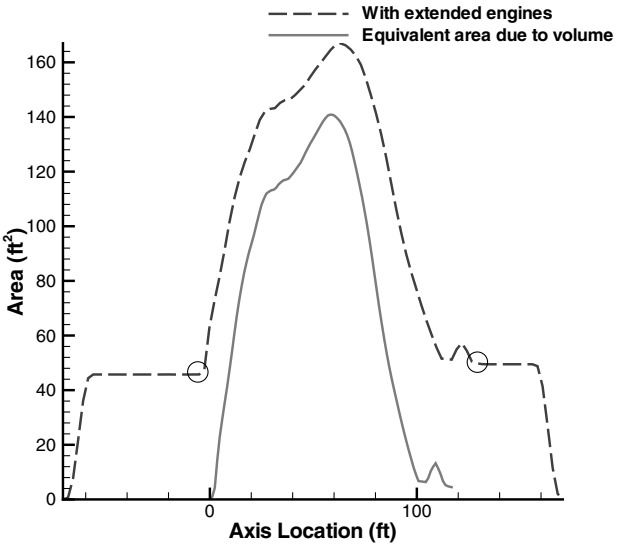

Fig. 11 Equivalent area due to volume for geometries with engines.

intersection region. An experienced AWAVE user can manually alter the geometry representation to match the area distribution if the final distribution is known by other means. However, this would mean more manual effort and the results would vary with the skill level of the user. Using GTS geometry based Mach-plane intersection, the equivalent area is computed without ambiguity because the geometry is treated as a single discretized configuration rather than a collection of various loosely placed components that can be moved by designers according to their convenience.

Including engine nacelles is more complicated than including wings and tails. Because the flow goes through the engines and not around them as for other components, the engine capture area has to be subtracted from the equivalent area due to volume. The axial locations where the engine contribution to the equivalent area starts and ends have to be computed exactly for a Mach number greater than 1. To do this accurately, the engine capture and exhaust portions are extended toward the front and rear of the nacelle, respectively, and then Mach planes are used to obtain the intercepted area of the whole aircraft including the extended nacelles. By doing this, regions of constant equivalent areas attributed only to the extended nacelles are obtained in the front and rear portions of the area distribution as shown in Fig. 11. The last axial location of the front constant area and the first location of the rear constant area region are computed and identified with circles (Fig. 11). The engine capture area is then subtracted from the area contribution and adjustments are made based on the prevailing angle of attack to yield the effective equivalent area due to volume as shown by the solid line (Fig. 11). If the inlet capture area is different from the exhaust area, the area distribution would have a nonzero contribution at the end. The small spike seen around 108 ft axial location is due to the combined contribution of the vertical and horizontal tails. The shift in the location of the rear spike from around 120 ft to 108 ft may be explained as follows: when the equivalent area due to volume is computed with the engines extended, the angle of attack is assumed to be zero. The angle of attack effects are included during the engine capture area subtraction stage. A positive angle of attack shrinks the equivalent area distribution to span a smaller region and increases the magnitude of the equivalent area. This idea is depicted in Fig. 12, where at a positive angle of attack the parallel Mach planes cut the aircraft in a smaller axial region when compared with the zero angle of attack case.

Design changes to reduce sonic boom usually increase aircraft drag. The main constituent of drag at supersonic regimes is the wave drag. The total wave drag includes a zero-lift portion and a lifting portion. In this study, only zero-lift wave drag is computed and any reference to wave drag from this point forward should be construed to be just the zero-lift wave drag component unless specified otherwise. The wave drag values computed using Mach planes intersecting the

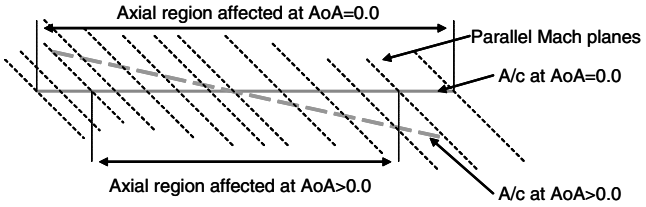

Fig. 12 Angle of attack effect on axial region.

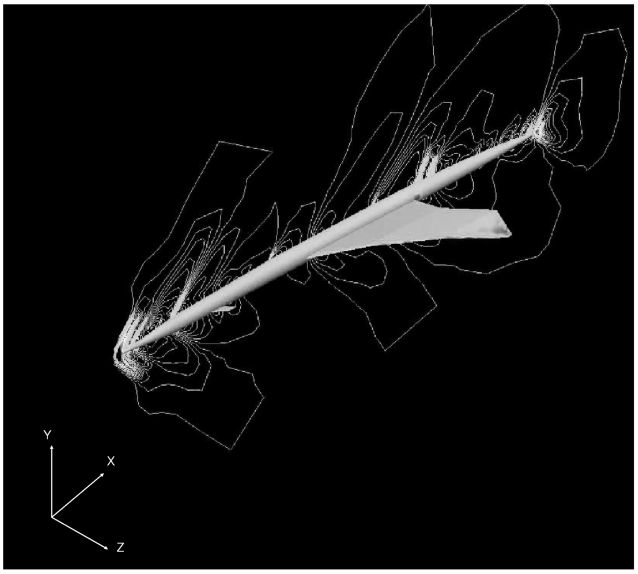

Fig. 13 Pressure contours obtained from a Cartesian CFD solver.

GTS-based geometry of the Sears–Haack body match values obtained via analytical expressions. It has been our observation that using less than 8 M plane cuts for azimuthal averaging on arbitrary geometries results in poor wave drag results using the GTS-based approach. In this study, we have used 16 M plane cuts in the computation of wave drag. The wave drag results over the geometry depicted in Fig. 9 are computed using traditional methods (AWAVE), a GTS-based method, and CFD. The GTS-based method used in this paper produces a zero-lift wave drag coefficient result (3.08) much closer to CFD (2.76), whereas AWAVE overpredicts this result (5.19); all the drag coefficients mentioned here are computed with a unit reference area. The difference in the drag values computed using the GTS-based approach compared with CFD is attributed to the linearized physics assumptions inherent in the GTS-based wave drag prediction.

B. Lift Contribution

In addition to volume effects, the estimation of equivalent area due to lifting effects is an important factor in predicting sonic boom. The lifting effects of the body are translated onto Mach planes to achieve this contribution. The lift analysis can use either a vortex lattice method, panel method, or a computational fluid dynamics simulation depending on the level of fidelity desired and the time available to the designer. In this study, a vortex lattice method [32] is used for lift contribution because of the computational time savings it offers.

Although CFD is not used in our optimization procedure, we demonstrate geometry transfer to a CFD solver using the configuration presented in Fig. 9. During the surface discretization stage, the neighboring triangle information is stored and supplied to a CFD solver. This information along with the surface grid allows the CFD preprocessor to quickly generate the volume mesh necessary for computing the flowfield. NASCART-GT [33] is used for this demonstration. It is a Cartesian grid Euler/Navier-Stokes solver with grid adaptation. Figure 13 shows the pressure contours after solution convergence for a Mach number of 1.4. The front bow shock, wing leading edge shock, trailing edge shock, and fuselage tail shock are seen in this figure. The solver was run in an explicit mode using Roe's flux vector splitting at a Courant, Freidricks, Levy number of 1.4 with grid adaptation turned on. The flow is assumed to be converged if the original residual is reduced by 10^{-6}. Traditionally CFD analysis over a complete aircraft requires a significant setup time where suitable grids are generated either manually or automatically. The approach used in this study has the potential to improve the geometry setup and grid generation aspects of the CFD flow solution process. Using the same geometry format for both CFD and linearized analyses allows the designer to pick the tool of choice depending on the computational resources available and the desired accuracy.

C. Addressing Atmospheric Uncertainty During Propagation

There is uncertainty associated with atmospheric pressure propagation because the calculated pressure signatures on the ground depend on various atmospheric properties prevalent during propagation. Atmospheric fluctuations cause variations in the pressure signature on the ground [34,35]. The major factors that affect sonic boom ground signatures are atmospheric temperature and wind distributions, atmospheric humidity distribution and atmospheric turbulence. Temperature distributions are a function of the lapse rates and the heights that separate the atmospheric layers. Lapse rate changes due to latitude, humidity, and seasonal changes from around $-5°\text{C/km}$ to about $-10°\text{C/km}$ compared to an average value of $-6.5°\text{C/km}$ for the standard atmosphere. An observation of weather balloon data reveals that the thickness of different atmospheric layers can vary and is uncertain. To model these effects without increasing the dimensionality of the problem, a set of meteorological shape parameters characterizing the temperature and wind distributions are chosen as shown in Table 4. The temperature gradients are specified by placing bounds on χ in Eq. (1). Thus, χ corresponding to each layer is used as a parameter instead of the actual temperature gradients. Standard atmosphere has a χ value of -0.6858×10^{-5} 1/ft in the lower atmosphere that corresponds to $-6.5°\text{K/Km}$. The ranges for all parameters are based on observations or predictions of the atmospheric profiles [36–38] at

Table 4 Meteorological parameters

Symbol	Description	Range
T1	Temperature at ground level	[52.33, 65.67]°F
HT1	Height of the temperature boundary layer	[951.44, 1017] ft
HT2	Height of the tropopause	[34996.7, 37181.8] ft
HT3	Height of the stratopause	[48665.8, 49759.4] ft
TL1	χ up to height HT1	$[3.048 \times 10^{-6}, 6.096 \times 10^{-6}]$ 1/ft
TL2	χ between HT1 and HT2	$[-0.86 \times 10^{-5}, -0.51 \times 10^{-5}]$ 1/ft
TL3	χ between HT2 and HT3	$[0.405 \times 10^{-6}, 0.81 \times 10^{-6}]$ 1/ft
HW1	Height of the wind boundary layer	[4429.1, 5413.4] ft
HW2	Second height for wind distribution	[26246.7, 29527.6] ft
HW3	Third height for wind distribution	[62335.9, 68897.6] ft
W1	Wind gradient near the ground to height HW1	[0.012, 0.025] 1/s
W2	Wind gradient between HW1 and HW2	[0.0035, 0.0042] 1/s
W3	Wind gradient between HW2 and HW3	[−0.0014, −0.0009] 1/s

various locations and seasons. Gaussian distributions around the standard atmospheric values are chosen for temperature profiles, whereas uniform distributions are used for calculating wind profiles.

$$\frac{T_2 - T_1}{H_2 - H_1} = T_1 \chi \tag{1}$$

The sonic boom impact at the ground level is measured using the perceived loudness level metric as it combines the effect of shock pressures, shock rise times, and signature duration of the ground pressure signature. References [39,40] show that perceived loudness level (PLdB) is the best metric to use in the subjective loudness evaluation of sonic booms. Further, Leatherwood and Sullivan [41] show that if the ground pressure signature has front shocks differing in strength compared with the rear shocks, the perceived loudness level is reduced. This signature asymmetry correction is included in this study to obtain the loudness levels values of the ground signatures.

A simple procedure to calculate a probabilistic estimate of the perceived sonic boom loudness when a single near-field signature is propagated through various atmospheric models is described here. Given the equivalent area distribution or the F function, propagation analysis (PCBOOM) is run for a fixed number of times with varying temperature and wind profiles according to the parameterization given in Table 4. The perceived loudness values for these cases are then used to fit a distribution using test statistic. The test [42,43] is one of the most powerful and important goodness-of-fit tests in the statistical literature especially for small sample sizes. This test is a modification of the Kolmogorov–Smirnov test. It weighs the tails more heavily and uses a hypothesized distribution resulting in a better goodness-of-fit test. Using the sample points, the parameters of the hypothesized distribution are estimated. Then a critical value of the test statistic corresponding to the hypothesized distribution is determined. Depending on the values of the test statistic and the critical values, the hypothesized distribution is accepted or rejected. AD^2 is defined in Eqs. (2) and (3) for a normal distribution.

$$AD^2 = -N - S_1 \tag{2}$$

where

$$S_1 = \sum_{i=1}^{N} \frac{(2i-1)}{N} \{\ell_n[F_0(x_i)] + \ell_n[1 - F_0(x_{n+1-i})]\} \tag{3}$$

If the mean and variance have to be estimated using the same data used for the test, then the test statistic is modified according to Eq. (4)

$$AD^2 = AD^2 \times \left(1 + \frac{4}{N} + \frac{25}{N^2}\right) \tag{4}$$

The critical value (CV) for a normal distribution is given by Eq. (5).

$$CV = 0.752 \Big/ \left(1 + \frac{0.75}{N} + \frac{2.25}{N^2}\right) \tag{5}$$

If $AD^2 > CV$, then the hypothesized distribution is rejected as not fitting the sample points. The critical and test statistic values are different for various distributions. In this study, the test has been used to accept or reject four possible distributions, normal, lognormal, Weibull, and exponential, due to their frequent occurrence in many statistical studies. After the distribution of the perceived loudness level has been obtained using the test, a cumulative distribution function (CDF) for that distribution is obtained. A value corresponding to any specified probability can be obtained from this CDF. Figure 14 depicts a sample CDF of the perceived loudness value along with a 95% probability estimate. The designer could choose the number of samples to use in the test. The higher the number of samples, the closer one can get to the actual CDF.

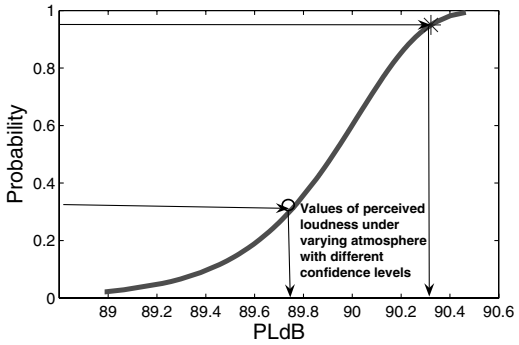

Fig. 14 Probabilistic perceived loudness level from cumulative distribution function.

IV. Other Analyses

This section briefly presents the other analysis tools used in this study in the evaluation of supersonic aircraft cruise performance and design.

A. Effect of Nacelle Interference

Nacelles cause the formation of shocks in the flowfield. There is a lip shock that is generated near the lip of the inlet and is propagated downstream. If the nacelle is directly under the wing, there are additional shocks in the near field due to shock reflection from under the wing. These shocks are manifested in a linearized method as additional equivalent area contributions [44]. Figure 15 shows the formation of shocks due to the nacelle under the wing as equivalent area contributions. The dashed lines represent the Mach planes cutting through the nacelle, the solid lines represent the shocks due to the engine inlet, and the dotted lines depict the shock reflections from the lower surface of the wing. There is a volume effect due to the thickness of the cowl and the inlet. Because of shock reflections, there is a lift effect that is shifted downstream compared with the volume effect. The result is the new solid curve (Fig. 15). The maximum magnitude of the solid curve is almost twice the maximum if the interference effects are not considered.

For a nacelle above the wing, the shocks are generated as before. However, these shocks are now partially shielded by the wing surface and do not contribute to the near field for sonic boom analysis if the three dimensional effects and diffraction are neglected. Figure 16 depicts the above reasoning in a simple sketch. The dashed lines are the Mach lines, the solid line are the shocks, and the dotted

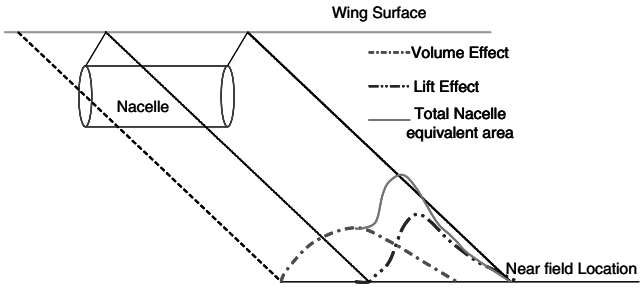

Fig. 15 Near-field signature with nacelle under the wing.

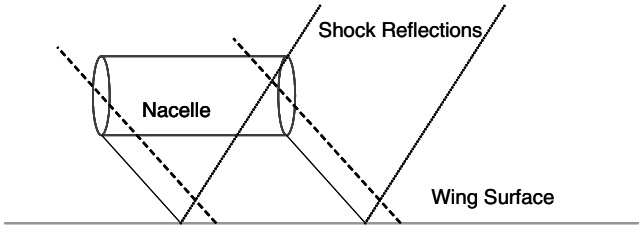

Fig. 16 Near-field signature with nacelle over the wing.

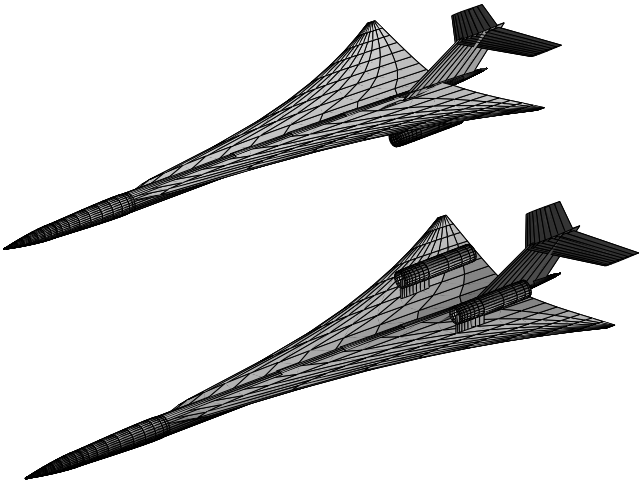

Fig. 17 Two configurations differing only in the nacelle location.

lines are the shock reflections from the top surface of the wing. If there is no surface to shield the shocks from the nacelles, the shocks contribute to the sonic boom near-field signature right under the aircraft.

To compare the nacelle interference effect, the configurations shown in Fig. 17 are used. All geometry features are the same except the location of the nacelles. Figure 18 compares the equivalent area distribution for both the configurations. Three different regions of interest are apparent. The first and second regions show the effect of area due to volume. An underwing nacelle causes a volume contribution at an earlier axial location compared with the volume contribution of an overwing nacelle, due to the Mach angle associated with the cutting planes. This is reflected in region 1, where the equivalent area computed for the geometry with below-wing nacelles is higher and in region 2, where the above-wing nacelle geometry has a higher area contribution. The reflected lift effects are seen in region 3, where the configuration with bottom nacelles has an increased area contribution. Because of the change in the area distribution, the pressure signature in the near field is different for the configurations considered. Figure 19 shows the comparison of the ground pressure signatures obtained using PCBOOM when standard atmospheric properties are considered during propagation. The overpressure magnitude for the nacelle underwing geometry is higher than the nacelle overwing geometry. This is due to the increased tendency for shock coalescence in the bottom nacelle case due to a forward location of the nacelle shocks. The rear shock

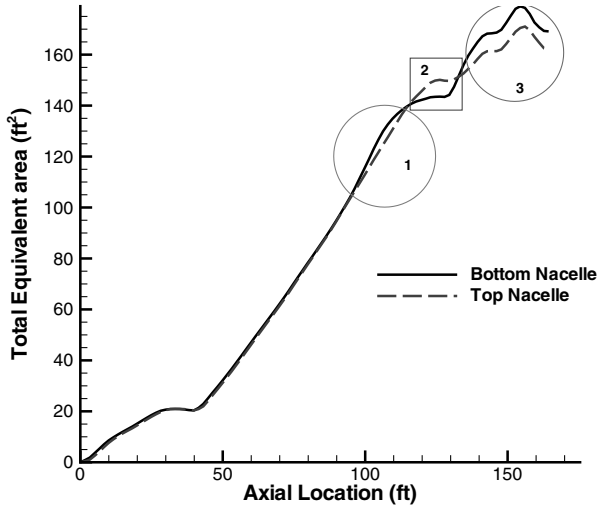

Fig. 18 Comparison of equivalent area for top and bottom nacelle configurations.

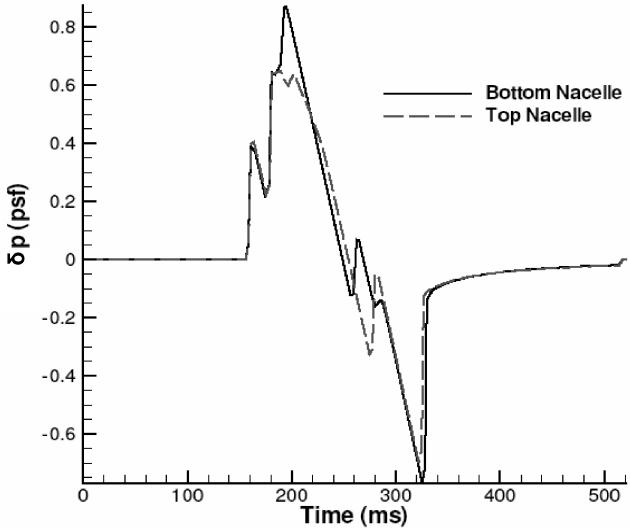

Fig. 19 Ground pressure signature comparison.

strength is increased for the nacelle under the wing designs due to shock reflection phenomenon.

B. Skin Friction Analysis

The skin friction calculation method uses the Eckert reference temperature method [45] for laminar flow and the van Driest II formula [46] for turbulent flow. Certain assumptions are made for the fluid properties including the flow recovery factor and the edge temperature for the laminar and turbulent flow cases. For the laminar case, the Chapman–Rubesin constant based on the reference temperature and Sutherland's viscosity law is computed. The local skin friction coefficient is based on the standard Blasius formula. For turbulent flow, the ratio of wall temperature to the adiabatic wall temperature is obtained for a specified edge Mach number and Newton's iterative method is used to obtain the incompressible equivalent of the friction coefficient

Once both laminar and turbulent skin friction coefficients are computed, a composite formula is used that computes the skin friction in the presence of transition from laminar to turbulent flow over the components. Transition locations are determined based on semiempirical relations relating to the onset of transition based on Reynolds' number (Re). A composite formula as shown in Eq. (6) is used for the combined skin friction drag coefficient (C_F) from the laminar (C_{Flam}) and turbulent (C_{Fturb}) components. The watertight geometry created using the GTS-based approach can easily provide accurate wetted areas and reference lengths.

$$C_F = C_{\text{Fturb}}(Re_L) - \left(\frac{x_c}{L}\right)[C_{\text{Fturb}}(Re_c) - C_{\text{Flam}}(Re_c)] \tag{6}$$

The above calculation does not include the effect of thickness. To account for thickness, form factors (FF) are used. For winglike shapes Eq. (7) provides the form factor, and for bodylike shapes Eq. (8) is used as the form factor.

$$FF = 1.0 + 2.7\left(\frac{t}{c}\right) + 100\left(\frac{t}{c}\right)^4 \tag{7}$$

$$FF = 1.0 + 1.5\left(\frac{d}{l_f}\right)^{1.5} + 50\left(\frac{d}{l_f}\right)^3 \tag{8}$$

V. Shape Optimization Results

The geometry generation and analyses tools discussed in the preceding sections are applied to optimize aircraft shape with the intent of simultaneously minimizing sonic boom loudness and

maximizing cruise efficiency. In the shape optimization process, the design variables are the shape parameters: $s_1, s_2, \ldots s_n$; $d_1, d_2, \ldots d_m$; aircraft length l; flight conditions: M, H; and cruise weight CW. For the purpose of this study, M and H have been arbitrarily fixed at 1.6 and 45000 ft, respectively. Although sizing the aircraft to perform a certain mission results in the weight of the aircraft, in this study we assume the cruise weight to be a design variable under the assumption that it satisfies the weight balance for a required mission.

A. Geometric Constraints

Suitable constraints are placed on certain variables to yield practical solutions. Some of the geometries created by the geometry engine might not be suitable for completing a given mission. The reasons might be that the wing volume may not be enough to hold sufficient fuel or the cabin volume is not adequate to provide comfortable seating to all the passengers. A typical mission for a supersonic business jet is takeoff, supersonic cruise, and landing with about 4000 nm of range. Following the conceptual analysis presented by Horinouchi [47], the fuel fraction needed to complete a typical mission is in the range of 0.4 to 0.55. In this study, to specify a constraint on the wing volume, a fuel fraction value of 0.4 is used. Based on the fuel fraction and cruise weight of the aircraft, the weight of the fuel required is obtained. With the knowledge of the density of the jet fuel used, the volume needed to carry that fuel is obtained. This volume, $0.007643 \times CW$ ft^3 is used as a lower limit for wing volume. Jet-A fuel with density 840 kg/m^3 is used in the above calculation. A cabin volume constraint is specified so that two crew and eight passengers are comfortably seated during the supersonic flight. Simple cabin sketches, seating arrangement, and dimensions specified by Horinouchi [47] are used to constrain the minimum cabin volume to be above 888 ft^3.

B. Flight Condition Constraints

Using the cruise weight of the configuration, the angle of attack required to maintain a steady level flight is iteratively obtained using the wing as the primary lift producing component. Because linearized methods are valid only for small angles of attack, if proper constraints are not placed, the optimizer would exploit this and produce shapes that would have to be flown at high angles of attack. To avoid this situation, an arbitrary upper limit of 4.0 deg has been placed on the angle of attack. The higher α_a, the lower is the effective length of the aircraft as shown in Eq. (9). If the length is 145.0 ft. and the angle of attack is 3 deg, the effective length is reduced to 135.32 ft. at a Mach number of 1.6. This is a considerable reduction in the effective length and will lead to less separation between front and rear shocks in the near-field signature and hence more intense sonic booms as the shocks have a greater chance to coalesce. To overcome this effect, the wings can be installed at an angle with respect to the fuselage so that sufficient lift is generated at lower angles of attack.

$$x_n = \frac{\sin(\mu - \alpha_a)}{\sin(\mu)} x \tag{9}$$

The optimization objectives are specified in Eq. (10). Two different conflicting objectives are used to achieve a Pareto-optimal front of configurations. The first objective is to minimize the perceived loudness $PLdB$ of the sonic boom signature before ground reflection. The second objective is to maximize the cruise lift to drag ratio C_L/C_D. However, unlike the sonic boom noise metric, this objective is a near-field phenomenon. Some of the side constraints used in the optimization are given in Table 5. The bounds for the variables are chosen to encompass a wide variety of aircraft shapes. Even though there are more geometric side constraints, only the representative ones are shown in the Table for the sake of brevity. The nonlinear constraints are given in Eq. (11).

Table 5 Some side constraints used in the optimization problem

Component	Variable	Lower bound	Upper bound
	Cruise weight, ft	90,000	130,000
Fuselage	Length, ft	100	160
	Cabin location, ft	30	45
	Cabin diameter, ft	7	12
	Cabin length, ft	35	50
	Diameter1 @ $0.04 \times l$, ft	2.2	3
	Diameter2 @ $0.15 \times l$, ft	7.2	7.6
	Diameter3 @ $0.30 \times l$, ft	7.2	8
	Diameter4 @ $0.65 \times l$, ft	7.2	7.6
	Diameter5 @ $0.75 \times l$, ft	4.5	6
	Diameter6 @ $0.92 \times l$, ft	2.2	3
Wing	Axial location, ft	35	60
	Aspect ratio	2	3.5
	Taper ratio	0.05	0.3
	Planform area, ft^2	2300	3100
	Sweep, deg	45	70
	Root t/c	0.025	0.045
	Tip t/c	0.025	0.035
	Dihedral, deg	0	10
	Root twist, deg	-2	2
	Tip twist, deg	0	5
	Strake sweep, deg	65	78
Horizontal tail	Aspect ratio	2	3.2
	Taper ratio	0.2	0.5
	Sweep, deg	−45	45
	Root t/c	0.03	0.05
	Dihedral, deg	−10	10
Vertical tail	Aspect ratio	0.8	1.2
	Taper ratio	0.4	0.7
	Sweep, deg	30	50
	Root t/c	0.03	0.06

$$\begin{aligned} &\text{Minimize}: \ PLdB(s_1, s_2, \ldots s_n, d_1, d_2, \ldots d_m, M, l, h, CW) \\ &\text{maximize:} \ \frac{C_L}{C_D}(s_1, s_2, \ldots s_n, d_1, d_2, \ldots d_m, M, l, h, CW) \end{aligned} \tag{10}$$

$$\begin{aligned} &\text{nonlinear constraints:} \ \alpha_a \le 4.0 \qquad P(PLdB \ge X) \le P_c \\ &\text{wing volume} \ge 0.007643 \times CW \ \text{ft}^3 \\ &\text{cabin volume} \ge 888.0 \ \text{ft}^3 \end{aligned} \tag{11}$$

The optimization tool used is a modified nondominated sorting genetic algorithm [48,49]. Classical genetic algorithm imposes a requirement that the design variables be encoded as binary strings. This means that the continuous design variables should be discretized, which may prevent the algorithm from finding true optimum. More binary bits can be used to improve the precision but the large string lengths cause an increase in the computational expense and reduction in operator efficiency. To overcome these problems, real encoding of the design variables is used in this study using BLX-α (blend crossover-α) operator as explained in Eshelman and Schaffer [50]. The BLX-α operator creates two offsprings from two parents using Eq. (12).

$$x_i^{(1:2,t+1)} = (1 - \gamma_i) x_i^{(1,t)} + \gamma_i x_i^{(2,t)} \tag{12}$$

where $\gamma = (1 + 2\alpha)u_i - \alpha$, $u_i = \text{rand}[0, 1]$ and α is a positive number to control the nature of the search. A value of 0.5 is used for α in this study. Following the crossover operation given by Buonanno and Mavris [7], a hierarchical crossover operation is used in this study. The standard uniform crossover is performed over two parent configurations if all the components are of the same category. However, if the components are dissimilar, then the components are

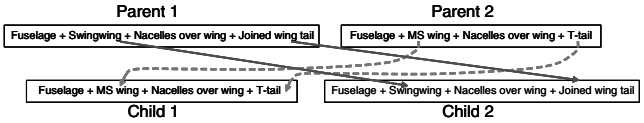

Fig. 20 Sample crossover sketch.

swapped with a probability of 0.5. Using this kind of crossover operation causes minimal gene disruption and leads to improved convergence rates. Figure 20 sketches the process where the swing-wing and joined-wing tail features of the first parent are swapped with the multisection wing and T-tail design of the second parent when creating offsprings. There is no crossover in the fuselage and pod settings.

C. Other Considerations

During the optimization process, for each aircraft shape, 100 different runs of the propagation algorithm, each with a different sample from the distributions of the atmospheric properties from Table 4, are conducted. These values are then used to fit a distribution as explained in Sec. III.C to obtain a probabilistic estimate of the perceived loudness value corresponding to $(1 - P_c)$ location on the cumulative probability distribution function. P_c represents a critical probability parameter. A value of 0.05 for P_c suggests that 95 out of 100 times, the perceived loudness value will be below the value predicted by the analysis model under varying atmosphere.

The tradeoff between boom strength and wave drag is very important. The wave drag of an aircraft is sensitive to the shape of the nose cone because the nose shape determines the strength of the front shock. To provide sufficient control near the nose, the geometry variables are chosen such that fuselage nose shapes include a NURBS surface (see Fig. 5), as well as a Sears–Haack half-body; Sears–Haack body is known to have the least wave drag.

To begin the shape optimization process, a random initial population of 150 members is created by the genetic algorithm. The population size was arbitrarily chosen to be around twice the number of shape variables, which as mentioned in Sec. II is roughly around 75. A variety of configurations with dissimilar shapes and sizes are obtained as the initial population. The ranges of the design variables and the constraints ensure that feasible geometries are generated. Constraints are handled using a modified method [49] during tournament selection phase. When two designs are picked for selection, depending on the constraints, these can be feasible or infeasible. There are three situations that need consideration. These cases along with their solutions are the following:

1) Both the solutions are feasible: In this case, the crowded distance comparison operator described by Deb [49] is used to pick one design over the other.

2) One design is feasible and the other infeasible: choose the feasible solution.

3) Both infeasible: choose the solution with a smaller overall constraint violation.

This constraint handling approach does not need the specification of any other penalty values or parameters.

D. Optimization Results

Figure 21 shows the shift of the populations as the generation number increases. In the first few generations, a rapid progression occurs followed by a slowly varying population toward the regions of desired objective values. The nondominated portion of the population after 25 generations is also shown in this figure. The estimate for $\frac{C_L}{C_D}$ does not include contributions from the wave drag due to lift, only zero-lift wave drag computed using the GTS-based method explained in Sec. III.A. This is the reason for high lift to drag ratios. In reality, these values are going to be smaller than those shown here. It is observed that the minimum loudness level has decreased from around 91.8 PLdB to around 87.9 PLdB. The loudness values are conservative estimates because they represent numbers that lie near the 0.95 probability on a cumulative

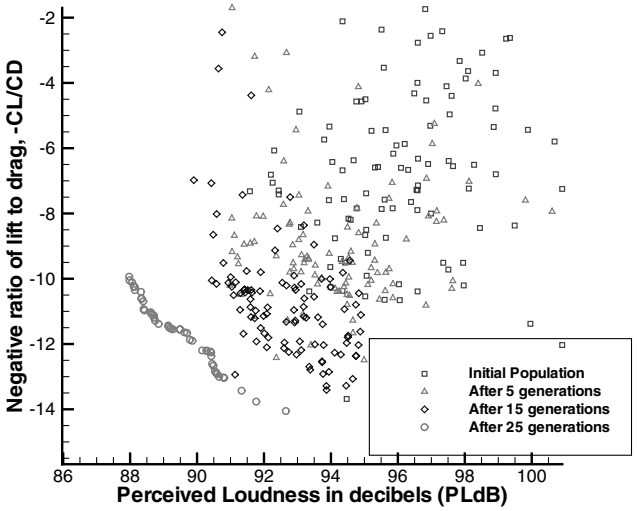

Fig. 21 Progression of populations through generations.

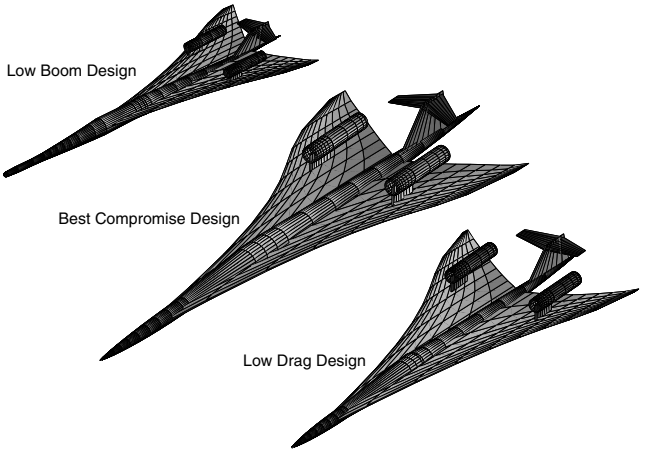

Fig. 22 Best designs from optimization.

distribution function. The optimization needs to be continued for more generations to realize further improvements in the objectives; however, further generations should be run using nonlinear aerodynamic analyses methods rather than improved linear methods used so far in the optimization runs. Continuing the optimization without improving the analyses may cause the optimizer to exploit the linear analyses or lead only to minor improvements in the desired objectives. A better approach would be continue the optimization using nonlinear CFD analyses as explained in Sec. III.B. This would be addressed in future research.

The best designs obtained after 25 generations are shown in Fig. 22. These include configurations with low sonic boom loudness, high $\frac{C_L}{C_D}$ ratio, and a configuration which falls approximately in the middle of the Pareto front between the low sonic boom design and the high $\frac{C_L}{C_D}$ design for this population at this stage of the optimization process. The low sonic boom and high $\frac{C_L}{C_D}$ designs are arbitrarily picked as endpoints of the midportion of the complete Pareto front. Table 6 provides the flight conditions, lift to drag ratio, and sonic boom loudness on the ground for the geometries shown in Fig. 22. The salient features of the compromise design along with some our observations are given below.

1) The nose region is slightly cambered down so that a downward propagating pressure signature sees a nose bluntness while the azimuthal average of the Mach-plane intercepted area is not too high. This prevents high wave drag values.

2) The engines are on top of the wings due to the favorable nature of nacelle interference as mentioned before. In this study, overwing

Table 6 Settings for the final designs

Configuration	α, deg	M	CW, lbs	Length , ft	Altitude, ft	$\frac{C_L}{C_D}$	PLdB
Low boom	1.95	1.6	93479.9	153.49	45000	11.04	88.12
Best compromise	1.8	1.6	96959.2	147.21	45000	11.51	89.65
Low drag	1.23	1.6	112336.28	140.41	45000	12.43	90.52

nacelles are preferred to underwing nacelles because of the beneficial effects of shock shielding for nacelles over the wing. This does not mean that overwing nacelle configurations are always superior to underwing nacelle configurations for sonic boom reduction. The analysis used in this study to account for nacelle interference is inadequate to model the beneficial effects of underwing nacelles. Reference [51] shows that wing reflexing offers a mechanism by which shock reflections from underwing nacelles are canceled. The decision to place nacelles above or below the wing cannot be correctly resolved using linearized analysis [52]. However, the optimizer may be modified to evaluate both overwing and underwing nacelle configurations by artificially penalizing the overwing configurations to a certain extent to account for the fact that some beneficial effects of underwing nacelles and some adverse effects (flow separation) of overwing configurations are not modeled. This was not done in the present study. An in-depth knowledge of the merits of over- and underwing nacelles would help immensely in assigning penalty factors.

3) The wing has a multisection configuration and allows for lift contribution along most of the aircraft length. Reference [53] shows this to be an important factor in reducing sonic boom loudness.

4) The design has a sweep-forward T-tail. This T-tail arrangement provides a medium to increase the effective length of the aircraft. If the T-tail is highly swept back, the equivalent area due to volume has a drop and rise in its distribution toward the rear region. This is because the wing contribution to the equivalent area ends and the T-tail contribution does not begin immediately. Therefore, in a small portion of the axial region, the only area contribution is from the vertical tail unless there are other components like nacelles that contribute to the equivalent area beyond the wing trailing edge. This drop and rise creates a nonsmooth equivalent area distribution toward the rear regions and leads to additional shocks in the far field. This situation is alleviated by either having a sweep-forward for the T-tail or placing nacelles in that area to overcome the drop in the equivalent area distribution. Each of these arrangements has consequences attached to it. By having a sweep-forward T-tail, the effective length of the aircraft is reduced and so the sonic boom ground signature could be concentrated over a smaller region increasing its overall loudness. Nacelle placement near the tail fills the equivalent area distribution to make it smoother, but the shock shielding advantages are lost.

E. Comparison of the New and Traditional Analyses Methods

In this section, the three configurations presented in Sec. V.D are analyzed using the traditional methods and the new analyses as described in this paper. Figures 23–25 depict the total (volume + lift) equivalent area distribution and the sonic boom signature before ground reflection using the traditional [12] and the new method for the low boom, best compromise and low drag designs, respectively. Traditional conceptual analyses produce an incorrect area distribution that results in an incorrect pressure signature on the ground. Traditional conceptual tools are limited by straight wing sections; this would cause the wing-fuselage and tail-fuselage intersections to be represented poorly, resulting in under- or overprediction of equivalent areas in these regions as shown in these figures. An experienced user can split and trim the geometry to produce better results using traditional tools. However, this human intervention and tweaking defeats the purpose of automated conceptual aircraft optimization. The new method represents the aircraft as a single entity by computing the wing-fuselage and other intersection regions similar to solid modeling techniques. This allows the new method to compute accurate equivalent area due to volume. A better lift analyses used in the new method allows for improved computation of the equivalent area due to lift. Even though for the configurations shown here, the traditional analyses overpredict the pressure perturbations in the ground signature, this need not be the case. Depending on the configuration, the traditional methods can underpredict these values.

As a final note, the sonic boom analysis and design conducted in this paper is limited to conceptual aircraft design purposes only. Realistic sonic boom signatures on the ground can be significantly modified and magnified or completely smeared due to gusts, vortical disturbances, thermal/entropy perturbations, or turbulence. This is a complicated dynamical phenomenon that requires advanced analysis. For a complete presentation of these advanced features, interested readers may refer to several experimental [54,55], numerical, and theoretical studies [56–58] on these issues. These effects have to be considered in the subsequent stages of design.

VI. Conclusions

A new design approach has been developed for sonic boom minimization based on improved linearized methods. The geometry

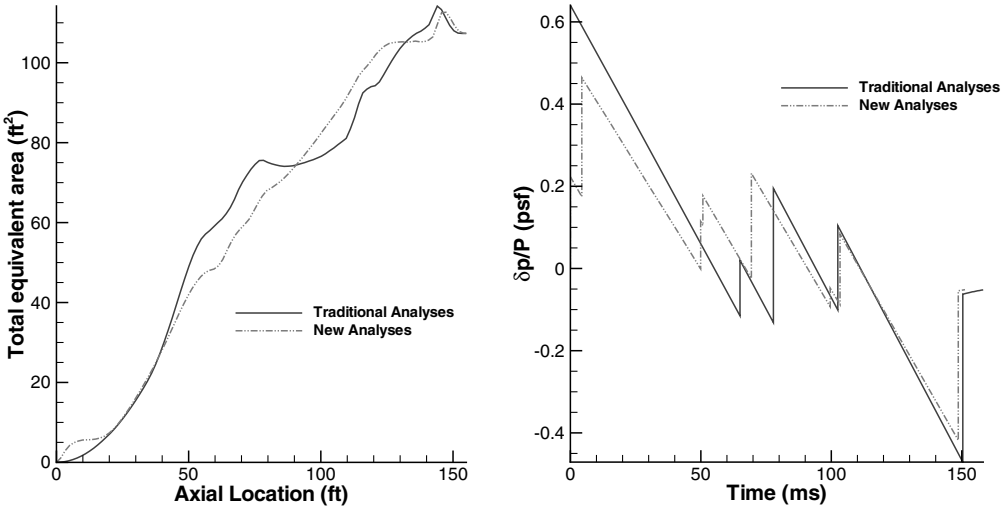

Fig. 23 Comparison of traditional and new analyses: low boom configuration.

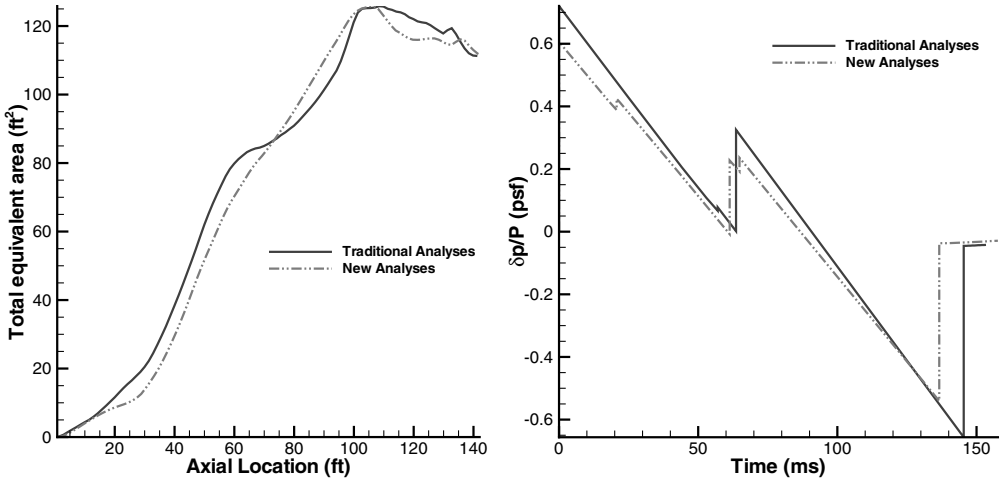

Fig. 24 Comparison of traditional and new analyses: best compromise configuration.

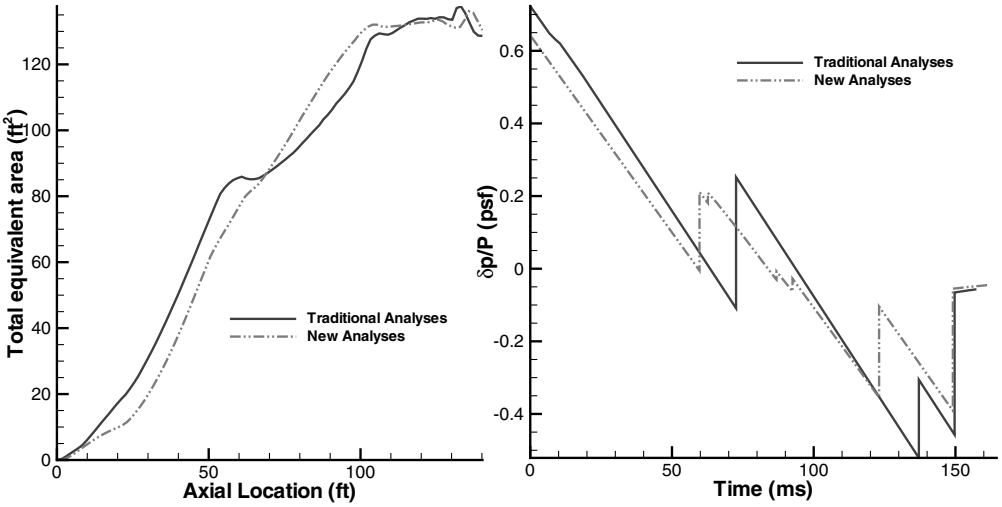

Fig. 25 Comparison of traditional and new analyses: low drag configuration.

generation and discretization procedure enables local shape control and an automatic way to combine linear and nonlinear analyses. The comparison of wave drag estimation demonstrated that a CFD method (NASCART/GT) and a traditional method (AWAVE) can be used over the same concept with no modifications to the geometry representation; the geometry preprocessing required for CFD is handled automatically by the new method. Traditional methods produce inaccurate equivalent areas due to their inherent geometry handling limitations driving the optimizer to undesirable places in the design space making the results unreliable. The new method is shown to produce accurate equivalent area due to volume along with the potential to run CFD analyses with minimal setup. This increases the designer's confidence in the results obtained. The use of varying atmospheric conditions in the prediction of perceived loudness levels on the ground allows the aircraft design process to better address atmospheric abnormalities that are encountered in actual operations.

Although the method is promising, much work needs to be done to accurately model nacelle interference, three dimensional lift, and advanced propagation effects to obtain practical configurations. High-fidelity analysis can capture the nonlinear near-field pressure signature better than linear methods, thereby improving the overall accuracy of the method. Furthermore, additional objectives such as range, center of gravity excursions, and takeoff and landing performance need to be included for a multidimensional set of optimal configurations. Finally, atmospheric absorption and relaxation effects need to be included in the pressure propagation to the ground level.

Acknowledgments

This work was supported under Grant NAG-1-02023, "Design Methodology for Revolutionary Aerospace Concepts," from NASA Langley Research Center with Craig Nickol as the technical monitor. We would also like to thank Stephane Popinet for developing the GNU triangulated surface library. This work would not have been possible without the valuable contributions and suggestions from Robert McDonald of Aerospace Systems Design Laboratory at Georgia Institute of Technology.

References

[1] Darden, C. M., "The Importance of Sonic Boom Research in the Development of Future High Speed Aircraft," *Journal of the National Technical Association*, Vol. 65, No. 3, 1992, pp. 54–62.

[2] Henne, P. A., "Case for Small Supersonic Civil Aircraft," *Journal of Aircraft*, Vol. 42, No. 3, 2005, pp. 765–774.

[3] Carlson, H., and Maglieri, D., "Review of Sonic Boom Generation Theory and Prediction Methods," *Journal of the Acoustical Society of America*, Vol. 51, No. 2, 1972, pp. 675–685.

[4] Seebass, R., "Sonic Boom Theory," *Journal of Aircraft*, Vol. 6, No. 3, 1969, pp. 177–184.

[5] Whitham, G., "The Flow Pattern of a Supersonic Projectile," *Communications on Pure and Applied Mathematics*, Vol. 5, No. 3, 1952, pp. 301–347.

[6] Aronstein, D. C., and Schueler, K. L., "Two Supersonic Business Aircraft Conceptual Designs, With and Without Sonic Boom Constraint," *Journal of Aircraft*, Vol. 42, No. 3, 2005, pp. 775–786.

[7] Buonanno, M. A., and Mavris, D. N., "A New Method for Aircraft

Concept Selection Using Multicriteria Interactive Genetic Algorithms," AIAA Paper 2005-1020, Jan. 2005.
[8] Mack, R. J., "A Supersonic Business-Jet Concept Designed for Low Sonic Boom," NASA TM 2003-212435, Oct. 2003.
[9] Harris, R. V., "An Analysis and Correlation of Aircraft Wave Drag," NASA TM X-947, April 1964.
[10] Craidon, C. B., "User's Guide for a Computer Program for Calculating the Zero-Lift Wave Drag of Complex Aircraft Configurations," NASA TM-85670, Nov. 1983.
[11] Hayes, W. D., Haefeli, R. C., and Kulsrud, H. E., "Sonic Boom Propagation in a Stratified Atmosphere with Computer Program," NASA CR-1299, April 1969.
[12] Coen, P. G., "Development of a Computer Technique for the Prediction of Transport Aircraft Flight Profile Sonic Boom Signatures," Master's Thesis, The George Washington University, March 1991.
[13] Rallabhandi, S. K., and Mavris, D. N., "Sonic Boom Minimization Using Improved Linearized Tools and Probabilistic Propagation," AIAA Paper 2005-1019, Jan. 2005.
[14] George, A. R., and Seebass, R., "Sonic Boom Minimization Including Both Front and Rear Shock Waves," *AIAA Journal*, Vol. 10, No. 10, 1969, pp. 2091–2093.
[15] Darden, C., "Sonic Boom Minimization with Nose-Bluntness Relaxation," NASA TP-1348, Sept. 1979.
[16] Plotkin, K. J., "PCBoom3 Sonic Boom Prediction Model: Version 1.0c," AFRL-HE-WP TR 2001-0155, Wyle Research Laboratories, Arlington, VA, May 1996.
[17] Thomas, C., "Extrapolation of Sonic Boom Pressure Signatures by the Waveform Parameter Method," NASA TN D-6832, June 1972.
[18] Mavris, D. N., and Delaurentis, D., "Methodology for Examining the Simultaneous Impact of Requirements, Vehicle Characteristics, and Technologies on Military Aircraft Design," *Proceedings of the 22nd Congress of the International Council on the Aeronautical Sciences*, International Council on the Aeronautical Sciences, Harrogate, U.K., 2000.
[19] Barger, R. L., and Adams, M. S., "Automatic Computation of Wing-Fuselage Intersection Lines and Fillet Inserts With Fixed-Area Constraint," NASA TM-4406, March 1993.
[20] Barger, R. L., and Adams, M. S., "Automatic Procedures for Computing Complete Configuration Geometry from Individual Component Descriptions," NASA TM-4607, July 1994.
[21] Stevens, S., "Perceived Level of Noise by Mark VII and Decibels(E)," *Journal of the Acoustical Society of America*, Vol. 51, No. 2, 1972, pp. 575–601.
[22] Bloor, M. I., and Wilson, M. J., "Efficient Parameterization of Generic Aircraft Geometry," *Journal of Aircraft*, Vol. 32, No. 6, 1995, pp. 1269–1275.
[23] Smith, R. E., Bloor, M. I., Wilson, M. J., and Thomas, A. M., "Rapid Airplane Parametric Input Design," AIAA Paper 1995-1687, June 1995.
[24] Kerr, P. A., Smith, R. E., and Posenau, M.-A. K., "GEOLAB Surface Modeling and Grid Generation Technology and Services," NASA 95-CP3291, May 1995.
[25] Samareh, J. A., "A Novel Shape Parameterization Approach," NASA TM-1999-209116, May 1999.
[26] Samareh, J. A., "Survey of Shape Parameterization Techniques for High-Fidelity Multidisciplinary Shape Optimization," *AIAA Journal*, Vol. 39, No. 5, May 2001, pp. 877–884.
[27] Popinet, S., "The GNU Triangulation Surface Library," 2005.
[28] Shewchuk, J. R., "Triangle: Engineering a 2-D Quality Mesh Generator and Delaunay Triangulator, " *Lecture Notes in Computer Science*, Vol. 1148, Springer–Verlag, London, U.K., 1996, pp. 203–222.
[29] Jones, R. T., "Theory of Wing-Body Drag at Supersonic Speeds," NACA Rept. 1284, Langley, VA, 1953.
[30] Mortenson, M. E., *Geometric Modeling*, Wiley Computer Publishing, New York, 1997, 2nd ed.
[31] Rallabhandi, S. K., and Mavris, D. N., "An Unstructured Wave Drag Code for Preliminary Design of Future Supersonic Aircraft," AIAA Paper 2003-3877, June 2003.
[32] Miranda, L. R., Elliott, R. D., and Baker, W. M., "A Generalized Vortex Lattice Method for Subsonic and Supersonic Flow Applications," NASA CR-2865, Nov. 1977.
[33] Marshall, D. D., "*Extending the Functionalities of Cartesian Grid Solvers: Viscous Effects Modeling and MPI Parallelization*," Ph.D. Thesis, Georgia Institute of Technology, School of Aerospace Engineering, Atlanta, GA, May 2002.
[34] Pierce, A. D., and Maglieri, D. J., "Effects of Atmospheric Irregularities on Sonic Boom Propagation," *Journal of the Acoustical Society of America*, Vol. 51, No. 2, 1972, pp. 702–721.
[35] Brown, J. G., and Haglund, G. T., "Sonic Boom Loudness Study and Airplane Configuration Development," AIAA Paper 1988-4467, Sept. 1988.
[36] Blumrich, R., Coulouvrat, F., and Heimann, D., "Meteorologically Induced Variability of sonic boom Characteristics of Supersonic Aircraft In Cruising Flight," *Journal of the Acoustical Society of America*, Vol. 118, No. 2, 2005, pp. 707–722.
[37] Avila, R., Vernin, J., and Sanchez, L. J., "Atmospheric Turbulence and Wind Profiles Monitoring with Generalized Scidar," *Astronomy and Astrophysics*, Vol. 369, No. 1, April 2001, pp. 364–372.
[38] Sutherland, L. C., and Bass, H. E., "Atmospheric Absorption in the Atmosphere up to 160 km," *Journal of the Acoustical Society of America*, Vol. 115, No. 3, 2004, pp. 1012–1032.
[39] Leatherwood, J. D., and Sullivan, B. M., "Loudness and Annoyance Response to Simulated Outdoor and Indoor Sonic Booms," NASA TN-107756, May 1993.
[40] Sullivan, B. M., and Leatherwood, J. D., "Subjective Response to Simulated Sonic Booms with Ground Reflections," NASA TM-107764, May 1993.
[41] Leatherwood, J. D., and Sullivan, B. M., "Effect of Sonic Boom Asymmetry on Subjective Loudness," NASA TM-107708, Dec. 1992.
[42] Stephens, M., "EDF Statistics for Goodness of Fit and Some Comparisons," *Journal of the American Statistical Association*, Vol. 69, No. 347, 1974, pp. 730–737.
[43] Stephens, M., "Goodness of Fit for the Extreme Value Distribution," *Biometrika*, Vol. 64, 1977, pp. 583–588.
[44] Mack, R. J., "A Numerical Method for Evaluation and Utilization of Supersonic Nacelle–Wing Interference," NASA TN D-5057, Feb. 1969.
[45] White, F. M., *Viscous Fluid Flow*, McGraw–Hill Publications, New York, 1974.
[46] Hopkins, E., "Charts for Predicting Turbulent Skin Friction From the Van Driest Method, Part II," NASA TN D-6945, Oct. 1972.
[47] Horinouchi, S., "Conceptual Design of a Low Boom SSBJ," AIAA Paper 2005-1018, Jan. 2005.
[48] Srinivas, N., and Deb, K., "Multiobjective Optimization Using Nondominated Sorting in Genetic Algorithms," *Evolutionary Computation*, Vol. 2, No. 3, Jan. 1995, pp. 221–248.
[49] Deb, K., Pratap, A., Agarwal, S., and Meyarivan, T., "A Fast and Elitist Multi-Objective Genetic Algorithm: NSGA-II," KanGAL Rept. 200001, IIT Kanpur, Kanpur, India, 2000.
[50] Eshelman, L., and Schaffer, J., "Real Coded Genetic Algorithms and Interval Schemata," *Foundations of Genetic Algorithms*, Vol. 2, Morgan Kaufman, San Mateo, CA, 1993, pp. 187–202.
[51] Morgenstern, J. M., "Tail-Braced Wing Aircraft and Configurations for Achieving Long Supersonic Range and Low Sonic Boom," United States Patent 20040056150, Lockheed–Martin, 2004.
[52] Howe, D. C., "Engine Placement for Sonic Boom Mitigation," AIAA Paper 2002-148, Jan. 2002.
[53] Ferri, A., and Ismail, A., "Effects of Lengthwise Lift Distribution on Sonic Boom of SST Configurations," *AIAA Journal*, Vol. 7, No. 8, 1969, pp. 1538–1541.
[54] Lipkens, B., and Blackstock, D. T., "Model Experiment to Study Sonic Boom Propagation Through Turbulence, Part 1: General Results," *Journal of the Acoustical Society of America*, Vol. 103, No. 1, Jan. 1998, pp. 148–158.
[55] Lipkens, B., "Model Experiment to Study Sonic Boom Propagation Through Turbulence, Part III: Validation of Sonic Boom Propagation Models," *Journal of the Acoustical Society of America*, Vol. 111, No. 1, Jan. 2002, pp. 509–519.
[56] Crow, S., "Distortion of Sonic Bangs by Atmospheric Turbulence," *Journal of Fluid Mechanics*, Vol. 37, No. 3, 1969, pp. 529–563.
[57] Plotkin, K. J., and George, A., "Propagation of Weak Shock Waves Through Turbulence," *Journal of Fluid Mechanics*, Vol. 54, No. 3, 1972, pp. 449–467.
[58] Bass, H. E., Layton, B., Bolen, L., and Raspet, R., "Propagation of Medium Strength Shock Waves Through the Atmosphere," *Journal of the Acoustical Society of America*, Vol. 82, No. 1, 1987, pp. 306–310.